Hierarchically porous nickel–cobalt phosphide nanoneedle arrays loaded micro-carbon spheres as an advanced electrocatalyst for overall water splitting application

Van Hien Hoa[a,1], Duy Thanh Tran[a,1], Huu Tuan Le[a], Nam Hoon Kim[a], Joong Hee Lee[a,b,*]

[a] Advanced Materials Institute of BIN Convergence (BK21 plus Global), Department of BIN Convergence Technology, Chonbuk National University, Jeonju, Jeonbuk, 54896, Republic of Korea
[b] Center for Carbon Composite Materials, Department of Polymer & Nano Science and Technology, Chonbuk National University, Jeonju, Jeonbuk, 54896, Republic of Korea

ABSTRACT

Due to the easy recyclability and pollution-free nature of hydrogen fuel, its highly purified production through electrochemical water splitting process has been attracting increasing attention. In this work, a hybrid of hierarchical porous nickel–cobalt phosphide nanoneedle arrays supported micro-carbon spheres was successfully synthesized and employed as robust bifunctional electrocatalyst for overall water splitting. The optimized Ni_1Co_3–P@CSs displayed catalytic activity with a low overpotential (η) of 57 mV at 10 mA cm^{-2} for hydrogen evolution and a η of 330 mV at 20 mA cm^{-2} for oxygen evolution, along with good stability after testing for 30 h. The water splitting cell of the Ni_1Co_3–P@CSs delivered smaller cell voltage at a current density of 50 mA cm^{-2} and much better durability than a similar device based on RuO_2/C and Pt/C. The enhanced performance was assumed to the unique hierarchical three-dimensional urchin nanostructure of bimetallic phosphide nanoneedles, which resulted in the synergetic effects to modulate electronic properties and electroactive surface area. These improved the reactant's intermediates adsorption energy, number of exposed active sites, and various shortened channels for charge transfer and reactant/electrolyte diffusion. Our finding offers an attractive electrocatalyst with low cost and high catalytic activity for efficient water electrolysis.

1. Introduction

Water splitting is the most promising route for large-scale hydrogen and oxygen production in sustainable energy conversion technologies. In this context, the electrochemical approach is an efficient and scalable solution, in which only water and electric energy are required to produce hydrogen. Theoretically, to effectively drive the electrochemical water splitting process at room temperature, a standard cell voltage of 1.23 V is necessary. However, a significant amount of additional energy is generally supplied in practice, and hence a high total energy of ~286 kJ mol^{-1} is required to obtain useful rates of the reactions. This issue has a remarkably negative impact on the cost and efficiency of the water splitting system. To address this issue, the development of advanced electrocatalysts, which are low in cost and high catalytic performance in terms of low overpotential (η), high current density (J), and long-term stability, has become a topic of great interest. The critical state-of-the-art electrocatalysts for electrochemical water splitting technologies have commonly been IrO_2/RuO_2- and Pt-based catalysts [1,2]. However, the expensive cost and natural inadequacy significantly limit their large-scale use for global applications. Recently, designing transition metal-based catalysts has been reported as a facile, cheap, and efficient approach [3,4]. Among these candidates, transition metal phosphides have emerged with extensive interest with their excellent catalytic activity [4], because the metal centers and phosphorous (P) sites in these materials can both work as highly active sites for the catalysis process [5]. Further, the relatively strong metal–P bonds can generate material with high thermal stability and hardness, as well as strong resistance to chemical attacks [2]. However, there are currently very few successful phosphide candidates available to be expected for simultaneously meeting the standards for practical activity and durability. Recently, both theoretical calculations and experimental works have shown that monometallic cobalt (Co)/nickel (Ni) phosphides exhibit promising activity for water splitting. This is due to their abundant active sites with reasonable surface adsorption energy as well as their

metallic nature without a band gap, which highly favor the electron transfer in catalysis [6]. In this context, Tian et al. successfully proposed a topotactic conversion reaction at low-temperature phosphidization in an effort to develop self-supported nanoporous CoP nanowire arrays, which offered good catalytic activity and stability over the large range of pH 0–14 [7]. Jung et al. reported a temperature-controlled synthesis of Ni_2P nanowires and Ni_5P_4 nanosheets on Ni substrates with vertical alignment and homogeneously exposed active sites, which exhibited outstanding catalytic performance toward overall water splitting [8]. The excellent activity and stability under harsh working environments were further pronounced for the formation of a bimetallic Ni–Co phosphide nanostructure with 50% increased conversion [9]. This was assumed to the synergistic effects from Ni–Co–P, which generate changes in the electronic structure and lower the surface adsorption energy for intermediates so as to be closer to the value on the Pt(1 1 1) surface, thereby providing high activity for water splitting [10]. An important factor was critically recognized in that the efficiency of the catalytic process toward HER and OER strictly relates to the surfaces of catalyst materials, which strongly depend on size, shape, dimensionality, and morphology. Therefore, constructing novel unique morphologies of catalysts or integrating them with a suitable supporting material has been attempted in order to expand their specific surface area as well as active site numbers so as to achieve the optimal performance of the catalyst material [11,12]. Regarding this aspect, some one-dimensional (1D), two-dimensional, and three-dimensional morphologies of phosphides, such as nanoneedles, nanowires, nanosheets, and nanoflower structures, have recently been investigated [10,13,14]. In particular, 1D phosphide nanostructure has received considerable research attention due to the large surface area, high roughness, and enhanced density of active sites to offer effectively catalytic behavior toward electrochemical reactions [15]. Besides, it also provided rich open space and porosity, diverse channels, and low crystal boundaries for fast charge/mass transport routes and easily chemical accessibility of electrolyte [16]. In this context, Li et al. developed Co–Ni–P nanowire arrays grown on Ni foam to catalyze H_2 and O_2 evolution with high-efficiency and ultra-stability over 3000 h [17]. Tang et al. reported a robust catalyst of Fe-doped CoP nanowire arrays on Ti foil, which possessed superior performance to previous nonprecious metal-based catalysts for water splitting under alkaline conditions [18]. For the fabrication of 1D electrocatalysts, the non-template approach has been employed [19]; however, the resulting structures tend to break down because of the rigorous gas bubbling and harsh working conditions during the HER/OER. Besides, even though the catalyst itself is conductive, the charge transfer ability between individual particles is still unsatisfactory, and eventually leads to poor catalytic activity. In order to address these disadvantages, the template approach has been widely developed by coupling catalyst with a supporting material, including metal-based supports (such as Fe_2O_3 spheres, TiO_2 spheres, Ti foil, Ni foam, and stainless steel) [17,18,20] and graphitic carbon supports (such as graphene, carbon nanotubes (CNTs), carbon fibers, or graphitic carbon nitrides), which possess excellent electrical conductivity, high surface area, and high structural stability for endowing the catalyst [21,22]. While plentiful results via template approach have been excitingly achieved, some issues also need to be solved. These relate to the high cost and complicated synthesis procedure due to the costly techniques, long-term processing, and expensive and toxic chemicals. In addition, the use of metal-based supports dramatically increases the weight of the entire device, thereby leading to lower overall specific energy density in the practical application. Recently, micro-carbon spheres (CSs) have been emerging as an interesting light support for various active catalysts. Compared to CNTs and graphene materials, large-scale CS synthesis can be quickly accomplished using sustainable, inexpensive, and environmentally friendly bio-resources [23–26]. More crucially, the porous characteristics, high mechanical properties, and the presence of oxygen functional groups formed on CSs' surface during

synthesis can facilitate the capture of metal cations, then efficiently improve the dispersity of the catalysts, further preventing aggregation of the catalyst materials [27–29]. In this study, we developed a newly designed aligned Ni–Co–P nanoneedle arrays supported CSs as an efficient bifunctional electrocatalyst for overall water splitting in alkaline medium. The optimized Ni_1Co_3–P@CSs electrocatalyst exhibited excellent performance for HER and OER. A real water splitting cell based on Ni_1Co_3–P@CSs was relatively superior to a system of RuO_2/C and Pt/C.

2. Experimental

2.1. Chemicals and material

Cobalt (II) nitrate hexahydrate ($Co(NO_3)_3 \cdot 6H_2O$, 99.9 wt%), nickel (II) nitrate hexahydrate ($Ni(NO_3)_2 \cdot 6H_2O$, 99.9 wt%), urea ($CO(NH_2)_2$, 99 wt%), glucose ($C_6H_{12}O_6$, 99 wt%), $NaH_2PO_2 \cdot H_2O$ (99 wt%), Pt/C catalyst (20 wt% with Pt particle diameter of 2.5–3.5 nm), and Nafion solution (5 wt%) were purchased from Sigma Co. (USA). Potassium hydroxide (KOH, ≥99.5 wt%) was purchased from Samchun Co. (Korea). Ultrapure water was prepared using the EYELA Still Ace SA-2100E1 (Tokyo Rikakikai Co., Japan) filtering system.

2.2. Preparation of CSs

The CSs were synthesized by a facile hydrothermal method, in which 8.0 g of glucose was dissolved in 60 mL DI water to form a homogeneous solution. The resulting solution was kept in an 80 mL Teflon-lined autoclave, which was treated at 190 °C for 7 h. The obtained black-brown precipitate was washed with DI water and ethanol for three times and then freeze dried for 10 h.

2.3. Preparation of Ni_1Co_3 hydroxide nanoneedle arrays on CSs (Ni_1Co_3–OH@CSs)

In a typical procedure, 60 mL of DI water containing 0.2 g of CSs was sonicated for 30 min to allow for the uniform dispersion of CSs. Then, 0.5 g of $Ni(NO_3)_2 \cdot 6H_2O$, 1.5 g of $Co(NO_3)_2 \cdot 6H_2O$, and 1.5 g of urea were dissolved into the solution under vigorous magnetic stirring. After stirring for 30 min, the obtained solution was moved into an 80 mL Teflon-lined autoclave for a hydrothermal process at 120 °C for 6 h. Upon completion of the reaction, the precipitates were washed with DI water/ethanol for three times, followed by freeze–drying for 10 h.

2.4. Preparation of Ni_1Co_3–P nanoneedle arrays on CSs

To obtain phosphide nanoneedle arrays supported CSs, 1 g of Ni_1Co_3–OH@CSs was put into a small boat, which was positioned at the center of a quartz tube of a quenching system under Ar atmosphere at 300 °C for 3 h with a heating speed of 3 °C min^{-1}. Next, 5 g of $NaH_2PO_2 \cdot H_2O$ was placed at the upstream side of the quartz tube, which was heated to 300 °C at a heating speed of 3 °C min^{-1} in Ar atmosphere. The sample was maintained at this temperature for 3 h before it was slowly cooled down to room temperature. For comparison, nickel phosphide (Ni–P@CSs), cobalt phosphide (Co–P@CSs), Ni_1Co_2–P@CSs, and Ni_1Co_4–P@CSs were also prepared.

2.5. Material characterization

The X-ray diffraction (XRD) was analyzed on a D/Max 2500V/PC (Rigaku Co., Japan) at the Center for University-Wide Research Facilities (CURF), Chonbuk National University, Korea. The XRD patterns of the materials were obtained using a Cu target (λ = 0.154 nm) in the 2θ range of 5–85° at a scan rate of 2° min^{-1}. Field-emission electron microscopy (FE-SEM) and energy dispersive X-ray analysis

(EDS) were performed on a Supra 40 VP instrument (Zeiss Co., Germany). Transmission electron microscopy (TEM) and selected area electron diffraction (SAED) were investigated using a JEM-2200FS instrument (JEOL Co., USA) operated at 120 kV, located at the Jeonju Center of the Korea Basic Science Institute. X-ray photoelectron spectroscopy (XPS) was recorded by a Theta Probe instrument (Thermo Fisher Scientific Inc., USA). The surface areas of the materials were investigated on an ASAP 2020 Plus system (Micromeritics Instrument Corp., USA).

2.6. Electrochemical measurements

The CHI 660D electrochemical workstation (CH Instruments Inc., USA) with a three-electrode system was used to test the electrochemical properties of the materials at room temperature. A rotating disk electrode (RDE, 0.071 cm^2 in diameter) deposited with catalyst powder, graphite rod, and Ag/AgCl served as working, counter, and reference electrodes, respectively. In order to prepare the working electrode, 3 mg of catalyst was dispersed in 0.5 mL of ethanol/nafion (v/v = 10:0.1) under sonication for 2 min. Next, the bare RDE, which had been carefully polished with alumina powder and rinsed with DI water several times to obtain a clean surface, was drop casted with 10 μL of catalyst solution, followed by drying under room temperature for 5 h prior to being used for electrochemical measurements. Linear sweep voltammetry (LSV) was applied in N_2-saturated 0.1 M KOH solution at the electrode rotation speed of 1600 rpm and the potential scan rate of 10 mV s^{-1} to obtain the catalytic behavior of the materials. The stability of the catalysts was measured by chronoamperometry at current densities of 10 and 100 mA cm^{-2}. Electrochemical impedance spectroscopy (EIS) was carried out from 0.1 to 10^5 Hz to evaluate the charge transfer ability of the catalysts. The electrochemical active surface area (ECSA) of the catalysts was assessed by cyclic voltammetry (CV) in a non-faradaic potential region (0.86–0.98 V) at different scan rates to achieve double layer capacitance (C_{dl}) value of the catalysts. The difference between anodic current density (J_a) and cathodic current density (J_c) at a given potential value was calculated. A plotted line based on ΔJ vs. the scan rate was built, and then fitted by a linear regression curve. The C_{dl} value calculated from the half of the slope of the fitting curve is consistent with the reactive surface area of the materials.

3. Results and discussion

3.1. Morphological and structural characterization

The synthesis procedures for preparing metal hydroxides, oxides, and phosphides are generally illustrated in Fig. 1a. The FE-SEM technique was employed to explore the surface morphology and microstructure of the catalysts. Fig. 1b shows morphology of the CSs simply prepared from glucose sources with uniform spherical shape and an average size of ∼ 1 μm. These CSs are expected to possess high surface areas, stable structures, and available oxygen-containing functional groups, which are highly useful for effectively supporting metal active catalyst materials [30,31]. Following the hydrothermal reaction for fabricating Ni–OH@CSs, Co–OH@CSs, Ni$_1$Co$_2$–OH@CSs, Ni$_1$Co$_3$–OH@CSs, and Ni$_1$Co$_4$–OH@CSs material, it can be seen that the Ni–OH@CSs was formed with Ni–OH nanoplatelets vertically oriented and fully covered on the surfaces of the CSs (Fig. S1a). Meanwhile, the Co–OH@CSs, Ni$_1$Co$_2$–OH@CSs, Ni$_1$Co$_3$–OH@CSs, and Ni$_1$Co$_4$–OH@CSs materials clearly exhibit similar morphological features, in which high density of aligned nanoneedle arrays are homogenously grown over the surfaces of the CSs (Fig. 1c and d; and Fig. S1c, e and g). In addition, the nanoneedles have diameter of 50 nm with the smooth external surface and sharp tip. After a simple phosphidization process at 300 °C, the morphology of the obtained materials perfectly retains the original characters of their hydroxide counterparts (Figs. 1e–g and S1b, d, f and h). High magnification images of the

nanoneedle surface further indicate the existence of significant roughness and porosity, which are beneficial for the penetration of electrolyte solution, charge transfer ability, and easy release of gas [32].

To further understand the microstructural characteristics of the materials, TEM and high resolution TEM (HR-TEM) were carried out. As shown in Fig. 2a and b, the Ni$_1$Co$_3$–P@CSs exhibits a hierarchical structure with thin nanoneedles perpendicular to surfaces of the CSs. The multi-crystalline nature of the material was revealed by SAED (inset in Fig. 2b). In addition, the HR-TEM image shows that an individual nanoneedle, which is formed by composing numerous ultra-small nanocrystals (∼ 5 nm), has an average diameter of around 50 nm. A highly porous architecture is also confirmed throughout each nanoneedle (Fig. 2c). Interestingly, HR-TEM images indicate that the crystalline state of the Ni$_1$Co$_3$–P NPs is surrounded by an amorphous phosphate layer due to the simultaneous occurrence of the phosphidization and decomposition of Ni$_1$Co$_3$–OH. In this regard, there is cooperation between the oxygen-containing gases released by the material and PH$_3$ evolved from the degradation of NaH$_2$PO$_2$ to react with NiCo surface and produce a NiCo-phosphates overlayer on the surface of NiCo–P nanocrystals [10,33]. This phenomenon is also proven with the high amount of phosphate groups detected by following XPS analysis (Fig. 3). As indicated by previous reports, the coverage of the NiCo–P nanocrystals with amorphous phosphate structure can effectively protect metal phosphide from some degree of detachment during the electrochemical operation. More importantly, it can promote the electron transfer from Ni$_1$Co$_3$–P to the phosphate structure for improving the catalytic behavior [10,33]. Fig. 2d and e confirm the uniform size of Ni$_1$Co$_3$–P NPs along with the presence of specific lattice fringes, correlated to the d-spacing of d(1 1 1) ∼ 0.22 nm of Ni–P [34] as well as d(1 1 1) ∼ 0.247 nm and d(0 0 2) ∼ 0.279 nm of Co–P crystal phase [35]. Fig. 2f–j shows the scanning transmission electron microscopy-high-angle annular dark field (STEM-HAADF) analysis together with the corresponding EDS element mapping. It indicates that Ni and Co element mainly concentrate at some parts of the nanoneedle, while the O and P element homogeneously distribute through the nanoneedle structure, further confirming the formation of NiCo–P covered by an amorphous phosphate structure. The EDAX spectrum quantitatively shows the availility of Ni, Co, P, C, and O signals, consistent with their content of 09.05, 26.91, 26.66, 12.52, and 24.86 in Ni$_1$Co$_3$–P@CSs material, respectively (Fig. 2k).

3.2. XRD, XPS, and BET analysis

The crystalline structures of the CSs, Ni$_1$Co$_3$–OH@CSs, Ni–P@CSs, Co–P@CSs, and Ni$_1$Co$_3$–P@CSs were confirmed by XRD characterization (Fig. 3a and b). The XRD pattern of the Ni$_1$Co$_3$–OH clearly shows the presence of a broad peak at 2θ of 19.7°, which is associated with d (0 0 2) plane of the graphitic CS. Other sharp peaks at 2θ of 17.48°, 33.8°, 35.4°, and 36.7°, 39.7°, 47.1°, 59.8°, and 62.1° relate to a crystalline mixture of both Ni$_2$(CO$_3$)(OH)$_2$ (PDF ≠ 35-0501) and Co (CO$_3$)$_{0.5}$(OH)$_{0.5}$ (PDF ≠ 48-0083) phase, as seen in Fig. S2 [36]. Following the phosphodization process, the crystal structure of metal hydroxide was efficiently converted into metal phosphide structure. In this regard, Ni–P@CSs exhibits a list of specific peaks consisting of Ni$_2$P (PDF ≠ 03-0953) and Ni$_5$P$_4$ (PDF ≠ 18-0883) crystal structure [37,38]. Meanwhile, the formation of Co–P@CSs is indicated by the availability of the peaks, suitable to crystalline characteristics of hexagonal CoP structure (PDF #29-0497) [39]. Regarding to the XRD pattern of the Ni$_1$Co$_3$–P@CSs, its diffraction peaks clearly belong to a mixture of crystals relating to Ni–P (Ni$_2$P and Ni$_5$P$_4$) and Co–P (CoP) phases.

XPS analysis was applied to investigative the surface chemistry of the as-synthesized materials. All materials show a small peak at 283.8 eV, which relates to the C1s binding energy of the graphitic carbon structure from CSs (Fig. 3c) [40]. In addition, the appearance of the P2p binding energy at 132.4 eV for Ni–P@CSs, Co–P@CSs, and Ni$_1$Co$_3$–P@CSs reveals the successful conversion from metal oxide to a
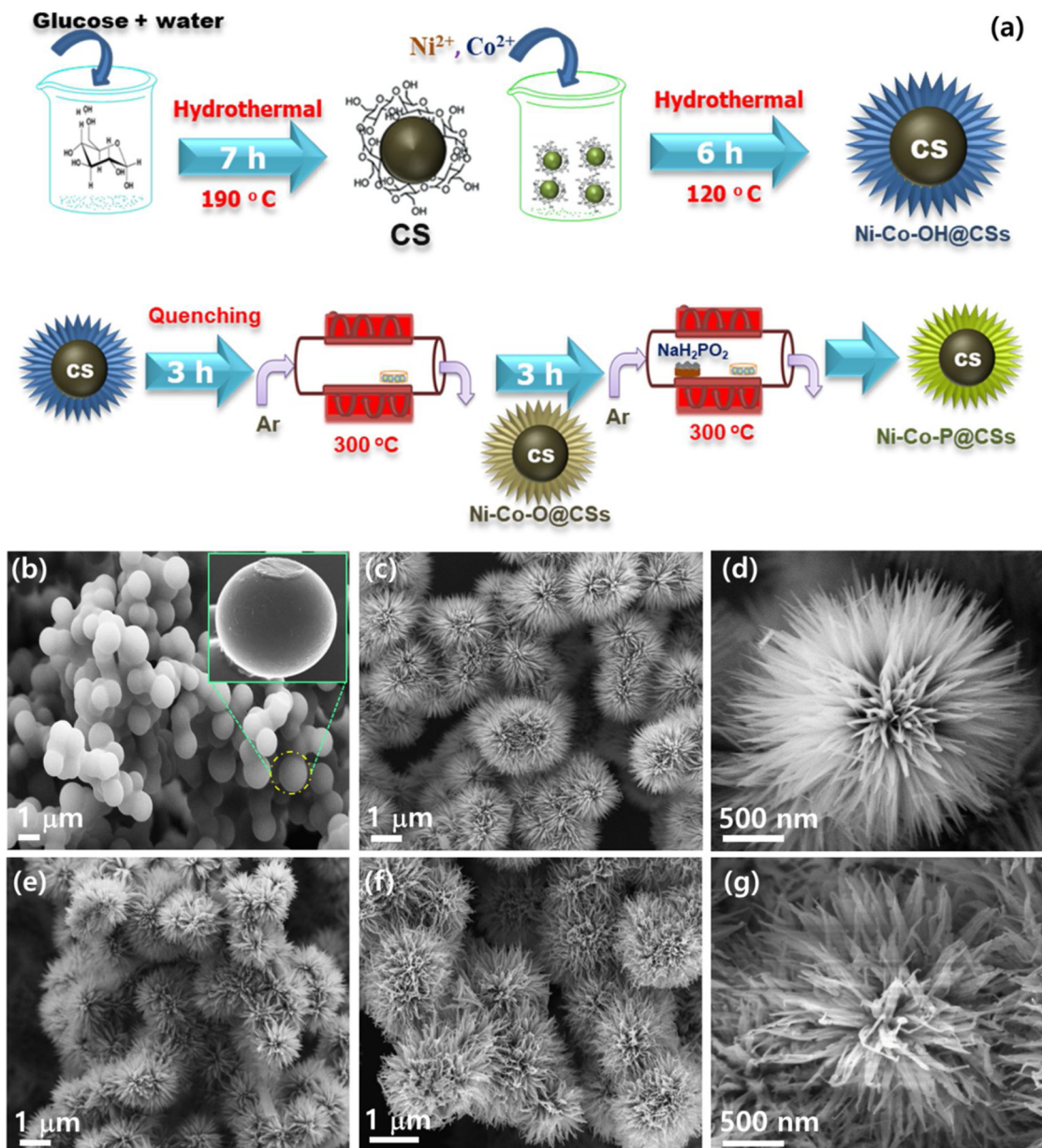
Fig. 1. (a) Schematic illustration for metal phosphide synthesis; (b) FE-SEM image of CSs (inset: high magnification image of a CS from Fig. 1b); (c, d) FE-SEM images of the Ni_1Co_3–OH@CSs at different magnifications; (e–g) FE-SEM images of the Ni_1Co_3–P@CSs at different magnifications.

metal phosphide structure. The high resolution Ni2p spectrum of the Ni_1Co_3–P@CSs clearly exhibits two doublets associated with $Ni2p_{3/2}$ and $Ni2p_{1/2}$ characteristics, as well as two shake-up satellites at 862.2 eV and 880.5 eV (Fig. 3d) [41,42]. In this context, the doublet at 853.8 and 871.0 eV is assigned to Ni–P [43]. Meanwhile, another doublet at 857.5 and 875.3 eV corresponds to the Ni–phosphate [10]. Similarly, the high resolution Co2p spectrum displays two peaks located at 779.1 eV and 793.9 eV as a result of the Co–P formation (Fig. 3e) [44]. Besides, two peaks available at 782.4 eV and 798.3 eV are due to the oxidized state of Co from Co-phosphate [45,46]. Furthermore, two satellite peaks of $Co2p_{3/2}$ and $Co2p_{1/2}$ are also observed at 786.0 and 803.1 eV, respectively. Fig. 3f shows the the binding energy of P2p in Ni_1Co_3P@CSs. There is one doublet at 129.2 eV and 130.1 eV correlated to the binding energy of $P2p_{3/2}$ and $P2p_{1/2}$ in the P–P bond, respectively. In addition, the presence of another peak located at 133.5 eV is corresponded to the phosphate species [47]. In the case of the high resolution O1s spectrum, it is deconvoluted into three peaks, consistent with Metal-O (O–Ni or O–Co in metal–PO_x phosphates) at 529.75 eV,

P–O (in PO_x phosphates) at 531.56 eV, and C–O/O–H from carbon sphere/adsorbed H_2O at 533.09 eV (Fig. S3) [48,49], further confirming the simultaneous presences of metal phosphide and metal phosphate structure in the resulting material. For the Ni–P@CSs and Co–P@CSs material, the similar characteristics of binding energy for Ni2p, Co2p, P2p, and O1s to those of Ni_1Co_3–P@CSs imply the formation of Ni–P and Co–P materials (Fig. S4).

The specific surface area of material is one of the most important parameters for evaluating its potential toward electrocatalytic applications. In this context, the nitrogen adsorption–desorption isotherms were applied to measure the surface area values of the prepared materials. The surface area of the Ni_1Co_3–OH@CSs, Ni_1Co_3–P@CSs, Ni–P@CSs, and Co–P@CSs was found to be 50, 60, 36, and 38 $m^2\,g^{-1}$, respectively (Fig. 4a). According to Barrett–Joyner–Halena (BJH) model, the pore size distribution of these samples is found in the range from 4 to 9 nm, indicating their mesoporous nature (Fig. 4b). In particular, the pore volume of the Ni_1Co_3–P@CSs is found to be significantly higher than that of the other materials, implying better exposure of the
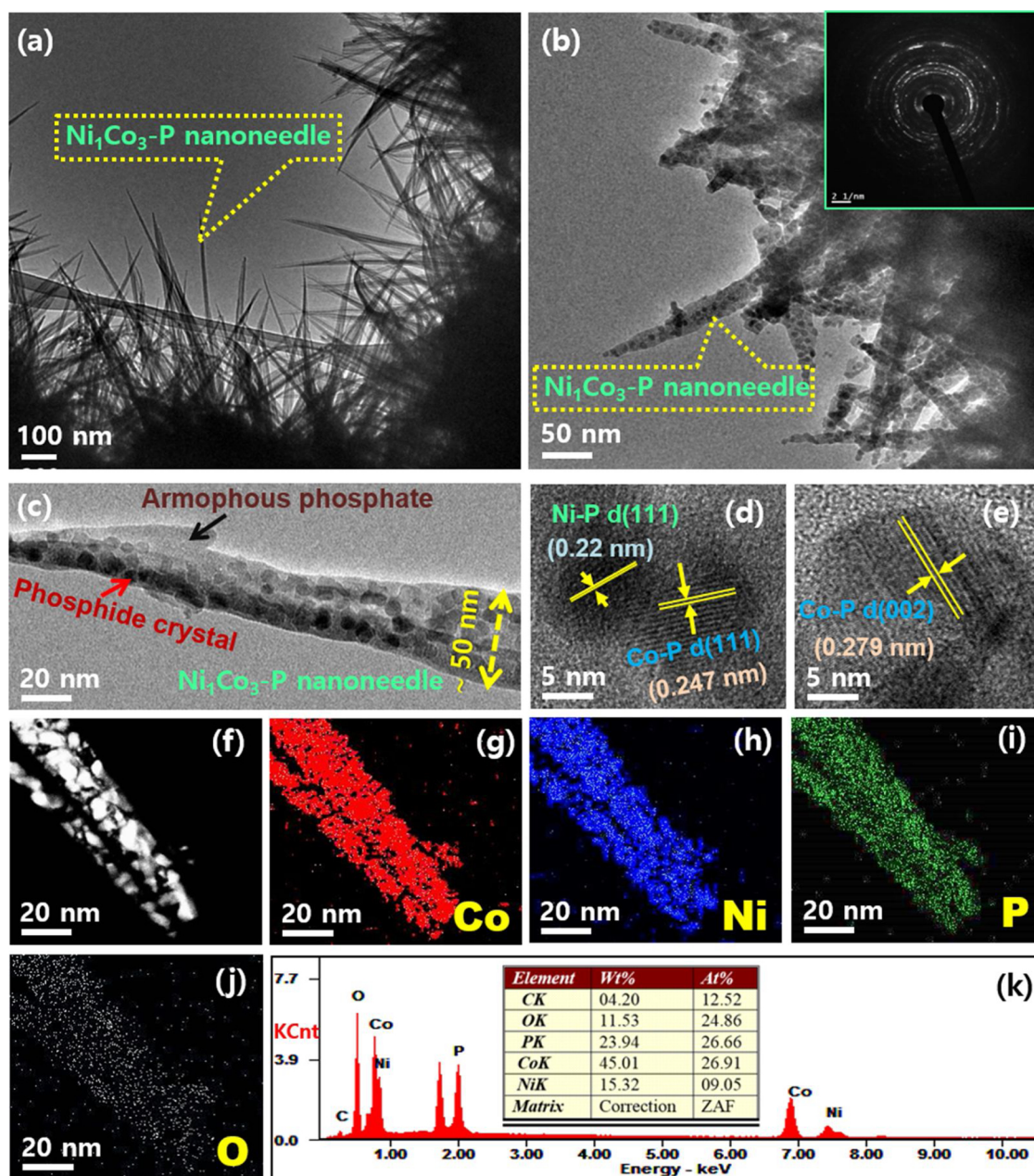
Fig. 2. (a, b) TEM and (c–e) HR-TEM images of Ni_1Co_3–P@CSs; (f) HAADF-TEM image of Ni_1Co_3P nanoneedle and the corresponding EDS element mapping of (g) Co, (h) Ni, (i) P, and (j) O; (k) EDAX result of the Ni_1Co_3–P@CSs.

catalytic active sites and larger surface area to facilite the catalytic activity, charge transfer ability, and electrolyte ion diffusion during catalysis process [50,51]. The surface area of the Ni_1Co_2–P@CS and Ni_1Co_4–P@CS were also investigated for comparison (Fig. S5). The results reveal surface area of 46 and $48\,m^2\,g^{-1}$ for the mesoporous Ni_1Co_2–P@CS and Ni_1Co_4–P@CS, respectively, smaller than that of the Ni_1Co_3–P@CS.

3.3. Electrocatalytic activity

3.3.1. HER activity

The electrocatalytic activity of the materials toward HER was investigated by LSV in 0.1 M KOH solution at a scan rate of $10\,mV\,s^{-1}$. The Ni_1Co_3–P@CSs exhibits excellent catalytic activity with a significantly lower η and higher J value than that of the Ni–P@CSs, Ni_1Co_2–P@CSs, Ni_1Co_4–P@CSs, Co–P@CSs, Ni_1Co_3–OH@CSs, and

Ni_1Co_3–O@CSs materials (Fig. 5a). In this context, the optimized Ni_1Co_3–P@CSs needs a small η of 57 mV to obtain a J value of $10\,mA\,cm^{-2}$. This is similar to Ni_1Co_2–P@CSs (57 mV), but substantially superior to that of the Ni–P@CSs (338 mV), Co–P@CSs (111 mV), and Ni_1Co_4–P@CSs (108 mV) (Fig. 5b). Comparing the HER activity between Ni_1Co_3–P@CSs and its hydroxide and oxide counterparts also shows a significantly lower η value of the Ni_1Co_3–P@CSs (Fig. 5c). In addition, the Ni_1Co_3–P@CSs delivers the highest J value of $140\,mA\,cm^{-2}$ at η of 500 mV among all the synthesized samples, further implying the superior behavior of the Ni_1Co_3–P@CSs toward the HER process. To gain insight into the catalytic HER behavior in terms of the electron/mass transport and the reaction kinetic, the corresponding Tafel slopes were calculated according to LSV measurements. As shown in Fig. 5d, the Tafel slope of the Ni_1Co_3–P@CSs is found to be $44\,mV\,dec^{-1}$, which is 75, 6, 4, 89, 129, and $84\,mV\,dec^{-1}$ less than that of the Ni–P@CSs, Ni_1Co_2–P@CSs, Ni_1Co_4–P@CSs, Co–P@CSs,
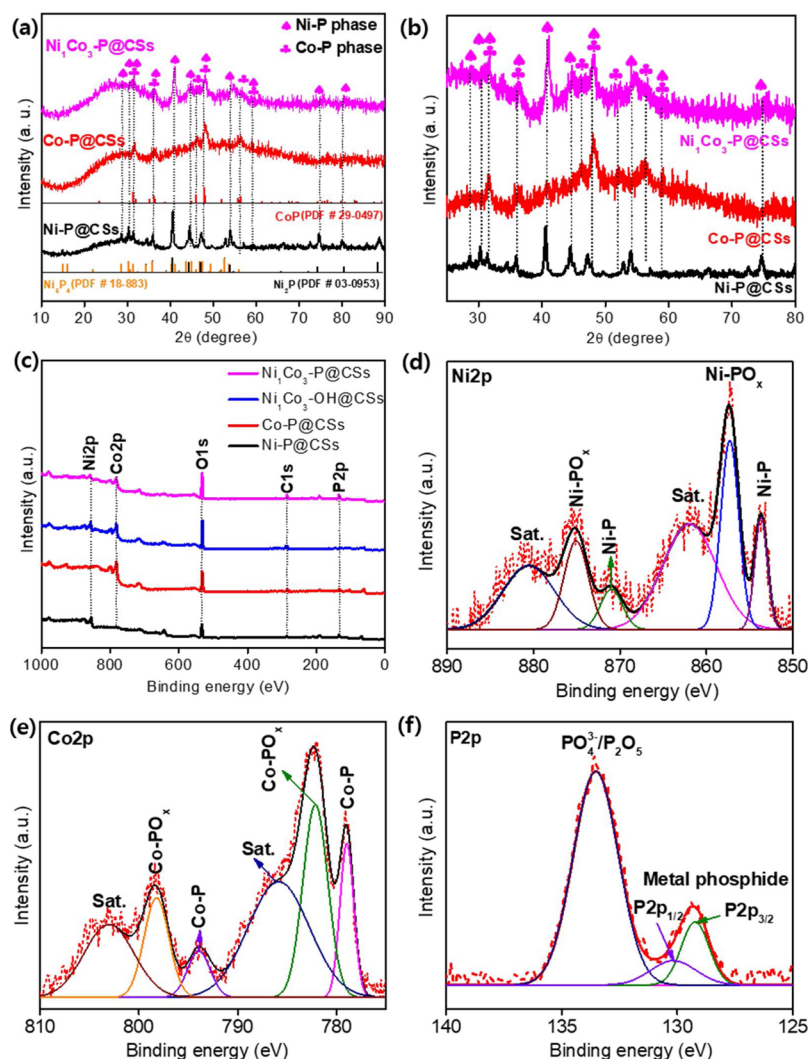
Fig. 3. (a, b) XRD patterns of different materials: Ni_1Co_3–P@CSs, Co–P@CSs, and Ni–P@CSs; (c) surveyed XPD spectra of different materials; high resolution XPS spectra of (d) Ni2p, (e) Co2p, and (f) P2p in Ni_1Co_3–P@CSs.

Ni_1Co_3–OH@CSs, and Ni_1Co_3–O@CSs, respectively. Interestingly, the Tafel slope value of the Ni_1Co_3–P@CSs reaches that of the Pt/C (33 mV dec^{-1}). This is due to the fact that the optimized combination of Ni, Co, and P can effectively modulate electronic properties at surface of the material, thereby improving the activity and amount of acceptor centers to be more favorable for H adsorption [52]. Under alkaline environment, the HER pathways consist of the H_2O adsorption, electrochemical separation of H_2O molecules into H_{ads} and OH^- species, and a subsequent desorption step. The Tafel slope is an intrinsic

characteristic of the catalyst that is decided by the rate-limiting step of the HER process. The determination of the Tafel slope is important for explanation of the elementary steps involved. In this context, the achieved Tafel slope of 33 mV dec^{-1} for the Pt/C suggests the HER on Pt surface occurs via a Volmer–Tafel mechanism [53]. Meanwhile, the Tafel slope of 44 mV dec^{-1} for the Ni_1Co_3–P@CSs suggests that an efficient HER is catalyzed via a Volmer–Heyrovsky mechanism, as demonstrated by earlier reports [54]. In this regard, the hydrogen production can be processed according to two reaction steps as described
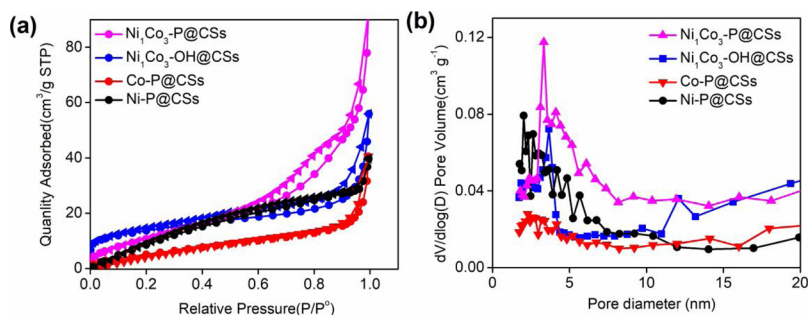

Fig. 4. (a) The nitrogen adsorption–desorption isotherms and (b) distribution of pore diameter for the Ni_1Co_3–P@CSs, Ni_1Co_3–OH@CSs, Ni–P@CSs, and Co–P@CSs materials.
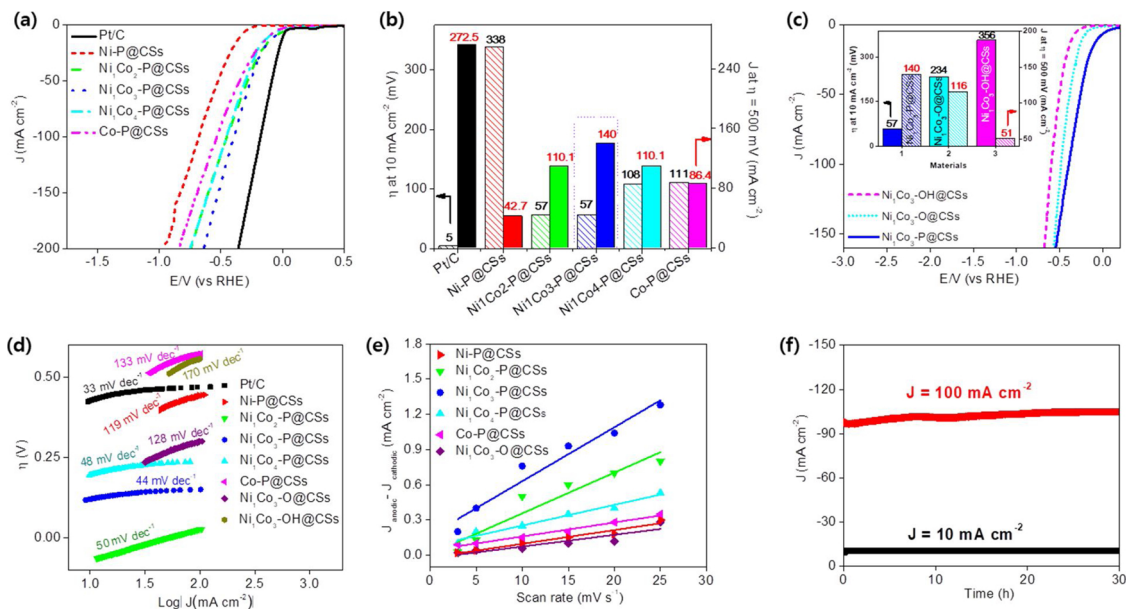
Fig. 5. (a) Polarization LSV curves and (b) overpotentials at J of 10 mA cm^{-2} and J at overpotential of 500 mV for Pt/C, Ni–P@CSs, Ni$_1$Co$_2$–P@CSs, Ni$_1$Co$_3$–P@CSs, Ni$_1$Co$_4$–P@CSs, and Co–P@CSs materials; (c) polarization LSV curves currents of Ni$_1$Co$_3$–P@CSs, Ni$_1$Co$_3$–O@CSs, and Ni$_1$Co$_3$–OH@CSs materials (inset: over-potentials at J of 10 mA cm^{-2} and J at overpotential of 500 mV for Ni$_1$Co$_3$–P@CSs, Ni$_1$Co$_3$–O@CSs, and Ni$_1$Co$_3$–OH@CSs); (d) Tafel plots of different materials; (e) capacitive J versus scan rate for different materials measured in the potential range from 0.86 to 0.96 V; (f) chronoamperometric measurement of HER at 10 mA cm^{-2} and 100 mA cm^{-2} using Ni$_1$Co$_3$–P@CSs as catalyst.

below:

(1) Volmer:

$$H_2 O + M^* + e^- = M^* - H_{ads} + OH^-$$

(2) Heyrovsky:

$$H_2 O + M^* - H_{ads} + e^- = H_2 + M^* + OH^-$$
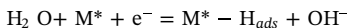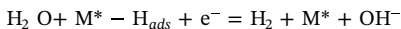
As a critical parameter, which critically influences the electro-chemical performance of the material, the electrochemically active surface area (ECSA) was assessed through evaluating the geometric double layer capacitance (C_{dl}) in a potential interval from 0.86 to 0.96 V at scan rates ranging from 2 to 25 mV s^{-1} (Fig. S6) [55]. Fig. 5e shows the significantly higher ECSA value of the Ni$_1$Co$_3$–P@CSs than that of the other materials; therefore, there is an enhanced number of exposed active sites and the diverse channels for charge transfer, ion exchangeability, and mass transfer ability, subsequently resulting in a significant improvement of catalytic performance. The stability of the Ni$_1$Co$_3$–P@CSs toward HER was measured by chronoamperometry at J of 10 and 100 mA cm^{-2}. In this regard, η at 10 mA cm^{-2} displays no distinct change, and η at 100 mA cm^{-2} shows a deflection of 6% after a long-term working time of 30 h. The stability of the Ni$_1$Co$_3$–P@CSs was also evaluated using LSV measurement by cycling 1000 times toward HER (Fig. S7). In this context, LSV result of the Ni$_1$Co$_3$–P@CSs after a 1000-cycle process does not shows significant change of η and J as compared to first cycle, further suggesting the good cycling stability of the 3D urchin architecture based on aligned Ni$_1$Co$_3$–P nanoneedle ar-rays supported CSs for HER. The morphology, structure, and composi-tion of the Ni$_1$Co$_3$–P@CSs after stability test were investigated. The SEM image (Fig. S8a) shows that the material well retains its original morphology and structure, in which abundance of uniform Ni$_1$Co$_3$–P nanoneedles vertically attaches on the surface of CSs. The presence of all elements in Ni$_1$Co$_3$–P@CSs structure is confirmed without sig-nificant change of their amount after long-term operation (Fig. S8b).

According to the achieved results, it can be concluded that the ad-mirable HER performance of the Ni$_1$Co$_3$–P@CSs can be resulted from some following reasons. Firstly, a unique 3D urchin nanoarchitecture increases electrocatalytic properties of active material. Secondly, the reasonable conversion of NiCo–OH to NiCo–P provides the improved

active sites for adsorbing H [10]. Thirdly, CSs have large surface and mechanical stability; therefore, the growth of 1D NiCo–P nanoneedles on CSs can minimize electrical resistance, as well as benefit its me-chanical and catalytic stability.

3.3.2. Electrocatalytic activity toward OER

The electrochemical behavior of the materials toward OER were evaluated by LSV in 0.1 M KOH saturated with N$_2$ gas at a scan rate of 10 mV s^{-1}. Fig. 6a shows the polarization curves of the Ni–P@CSs, Ni$_1$Co$_2$–P@CSs, Ni$_1$Co$_3$–P@CSs, Ni$_1$Co$_4$–P@CSs Co–P@CSs, and RuO$_2$/C catalyst. All the synthesized catalysts show a distinct anodic peak between 1.3 and 1.5 V, which is associated with the oxidation of Ni/Co (or both) species. Among the surveyed catalysts, the Ni$_1$Co$_3$–P@CSs exhibits earlier onset potential, smaller η at J of 20 mA cm^{-2}, and much greater J at η of 500 mV than that of the Ni–P@CSs, Ni$_1$Co$_2$–P@CSs, Ni$_1$Co$_4$–P@CSs, Co–P@CSs, and RuO$_2$/C (Fig. 6b). Similar results are also observed when the catalytic behavior of the Ni$_1$Co$_3$–P@CSs is compared to that of the Ni$_1$Co$_3$–OH@CSs and Ni$_1$Co$_3$–O@CSs (Fig. 6c). The η value at 20 mA cm^{-2} is found to be 330 mV for Ni$_1$Co$_3$–P@CSs, which is 180, 360, 50, 50, 130, 330, and 400 mV less than that of the RuO$_2$/C, Ni–P@CSs, Ni$_1$Co$_2$–P@CSs, Ni$_1$Co$_4$–P@CSs, Co–P@CSs, Ni$_1$Co$_3$–O@CSs, and Ni$_1$Co$_3$–OH@CSs, respectively. In addition, a comparison of η at higher current densities, including 50 and 100 mA cm^{-2} also exhibits the significant smaller overpotential of the Ni$_1$Co$_3$–P@CSs as compared to RuO$_2$/C, Ni–P@CSs, Ni$_1$Co$_2$–P@CSs, Ni$_1$Co$_4$–P@CSs, Co–P@CSs, Ni$_1$Co$_3$–O@CSs, and Ni$_1$Co$_3$–OH@CSs (Fig. S9). Regarding the current response toward OER, the J value of the Ni$_1$Co$_3$–P@CSs at an overpotential of 500 mV is 57 mA cm^{-2}, much superior to other synthesized materials. The electrocatalytic kinetic of the synthesized materials toward OER was investigated using the cor-responding Tafel plots (Fig. 6d). The Tafel slope of the Ni$_1$Co$_3$–P@CSs is 113 mV dec^{-1}, which is much smaller than that of the Ni–P@CSs (246 mV dec^{-1}), Ni$_1$Co$_2$–P@CSs (153 mV dec^{-1}), Ni$_1$Co$_4$–P@CSs (178 mV dec^{-1}), Co–P@CSs (234 mV dec^{-1}), Ni$_1$Co$_3$–O@CSs (231 mV dec^{-1}), and Ni$_1$Co$_3$–OH@CSs (210 mV dec^{-1}). In addition, the Tafel slope of the Ni$_1$Co$_3$–P@CSs is significantly smaller than that of the RuO$_2$/C (277 mV dec^{-1}), suggesting its superior OER kinetics. The obtained results are assumed to the formation of a unique 3D urchin
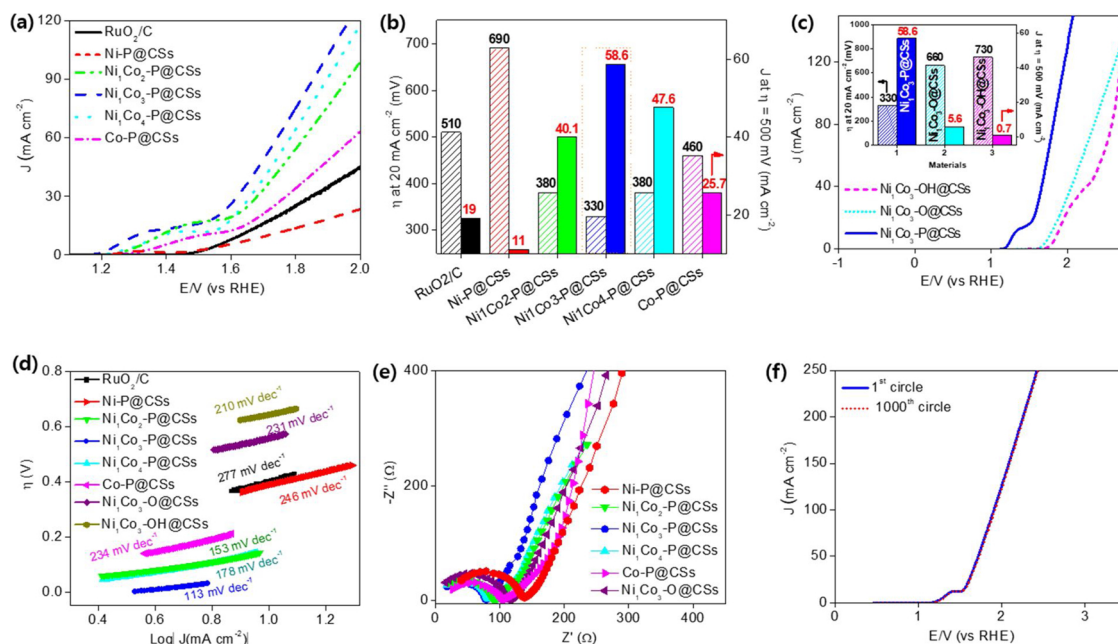
Fig. 6. (a) Polarization LSV curves and (b) η at J of 20 mA cm^{-2} and J at η of 500 mV for RuO$_2$/C, Ni–P@CSs, Ni$_1$Co$_2$–P@CSs, Ni$_1$Co$_3$–P@CSs, Ni$_1$Co$_4$–P@CSs, and Co–P@CSs materials; (c) polarization LSV curves currents of Ni$_1$Co$_3$–P@CSs, Ni$_1$Co$_3$–O@CSs, and Ni$_1$Co$_3$–OH@CSs materials (Inset: overpotentials at J of 20 mA cm^{-2} and J at η of 500 mV for Ni$_1$Co$_3$–P@CSs, Ni$_1$Co$_3$–O@CSs, and Ni$_1$Co$_3$–OH@CSs); (d) Tafel plots of different materials; (e) EIS measurements for different materials measured at -0.4 V in a frequency range from 10^{-2} to 10^5 Hz; (f) LSV measurement of Ni$_1$Co$_3$–P@CSs-based electrode toward OER at first cycle and 1000th cycle.

morphology, in which a reasonable combination of Co–Ni–P with an optimized ratio at nanoscale effectively improves the charge transfer and modulates the available surface-active sites. In this regard, the resulting phosphide catalyst can decrease the thermodynamic wall of the proton-coupled-electron transmission pre-equilibrium and boost the creation of O–O bonding, thereby reducing the activation energy essential for OER process [10,56]. Furthermore, the increase in ECSA as shown by the C_{dl} measurements in Fig. 5e suggests more exposed active sites of oxyhydroxides in situ created during the OER [10]. These oxyhydroxides are believed as the critical components of nickel cobalt phosphide to promote OER performance [57,58]. To further understand the alternation of composition at the surface of catalyst after the OER, the XPS analysis was conducted (Fig. S10). It can be seen that the Ni–P and Co–P peaks in the fresh sample become weak intensity. Meanwhile, the post-stabilized sample shows an increase of peaks relating to oxidized Ni (Ni–O) and Co (Co–O), which are originated from oxyhydroxides. Besides, the intensity of P2p also becomes very weak. These achievements imply that the surface-bound metal–PO$_x$ and metal–P of the Ni$_1$Co$_3$–P are oxidized to oxyhydroxides during catalyzation [47], thereby boosting the electron transmit from the metal–P to the external surface layer [59] and consequently contribute to the OER performance.

To further realize the reasons for the differences in catalytic behavior among the synthesized materials, EIS measurement at an applied potential of -0.4 V was investigated. The charge transfer resistance (R_{ct}) obtained from the semicircle in the high-frequency range is connected to the phenomenon at the interfacial region between the catalyst and the electrolyte.

Fig. 6e shows that Ni$_1$Co$_3$–P@CSs hybrid delivers a R_{ct} of only 65 Ω, which is lower than that of the Ni–P@CSs (109 Ω), Ni$_1$Co$_2$–P@CSs (85 Ω), Ni$_1$Co$_4$–P@CSs (76 Ω), Ni–P@CSs, Co–P@CSs (84 Ω), and Ni$_1$Co$_3$–O@CSs (110 Ω). The low R_{ct} value of the Ni$_1$Co$_3$–P@CSs reveals a fast electron transfer rate at the electrode/electrolyte interface due to the synergistic effect resulting from its unique hierarchical nanostructure, thereby providing an important contribution for its improved catalytic performance. The stability of the Ni$_1$Co$_3$–P@CSs-based

electrode toward OER was examined by LSV after an extensive cycling process (Fig. 6f). The obtained LSV curves indicate that the overpotential required to maintain a constant J of 10 mA cm^{-2} does not show any noticeable change after 1000 cycles. The morphology and structure of the Ni$_1$Co$_3$–P@CSs after long-term OER operation were also studied. Fig. S11a confirms the good stability of the urchin structure with the dense Ni$_1$Co$_3$–P nanoneedles vertically attaching on whole surface of CSs. Interestingly, Fig. S11b shows a significant change of O and P concentration in hybrid after stability test as compared to those of a fresh one, in agreement with XPS analysis from Fig. 10. In this context, the increase of O and the reduction of P amount in the hybrid's structure suggest the formation of more exposed active sites based on oxyhydroxides, which have been revealed as an important factor to accelerate OER activity.

To further understand the important effect of the CSs support on the catalytic activity of the synthesized metal phosphide material, a pure Ni$_1$Co$_3$–P sample was prepared without using CSs support and the catalytic HER and OER of the Ni$_1$Co$_3$–P was compared to those of the Ni$_1$Co$_3$–P@CSs under same operation conditions. It can be seen that the Ni$_1$Co$_3$–P@CSs exhibits superior HER (Fig. S12a) and OER (Fig. S12b) in terms of overpotential and current response to those of the pure Ni$_1$Co$_3$–P material, indicating the effective role of the CSs for supporting Ni$_1$Co$_3$–P nanoneedles to enhance their performance toward water splitting. The catalytic behavior of the optimized catalyst was compared with the recently reported catalysts as seen in Table S2, which demonstrates that the Ni$_1$Co$_3$–P@CSs can be considered one of the top tier earth-abundant catalysts currently available.

3.3.3. Practical water splitting application

Regarding the practical application of the Ni$_1$Co$_3$–P@CSs toward overall water splitting, the Ni$_1$Co$_3$–P@CSs-based electrodes were used as the anode and cathode in a water electrolysis system (Fig. 7a). The cell voltage of the Ni$_1$Co$_3$–P@CSs (+)//Ni$_1$Co$_3$–P@CSs (−) and RuO$_2$/ C (+)//Pt/C (−) at J of 50 mA cm^{-2} in 0.1 M KOH solution was found to be 1.54 V and 1.58 V, respectively, demonstrating the superior behavior of our catalyst to that of the commercial product (Fig. 7b). This
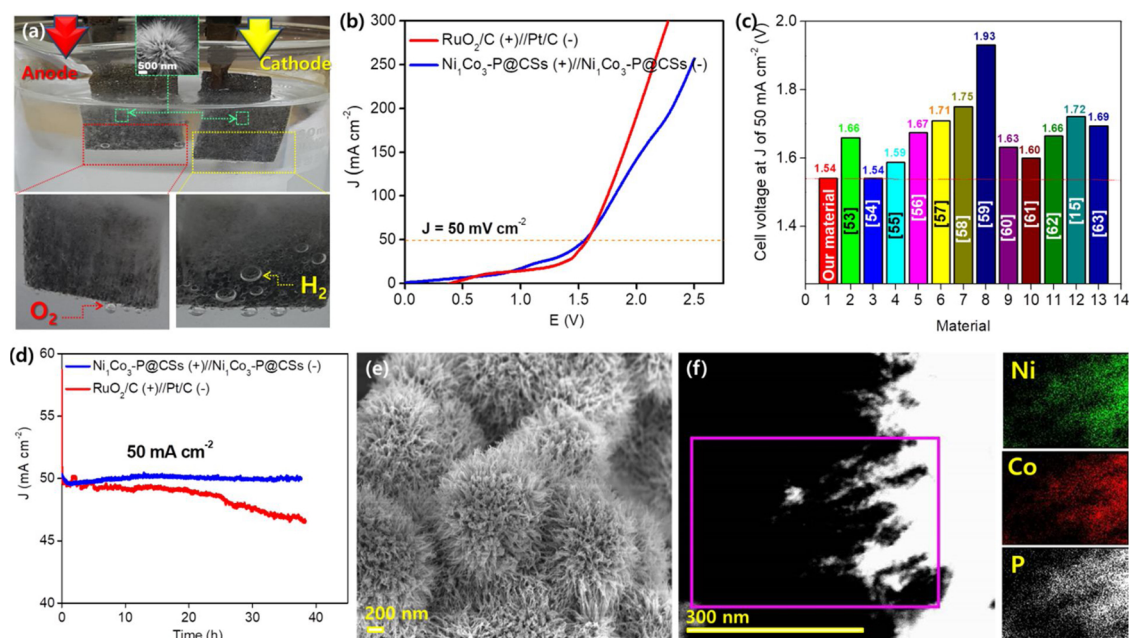
Fig. 7. (a) Photograph of the two-electrode electrolyzer using $Ni_1Co_3P@CSs$ as both anode and cathode at an applied potential of 1.54 V; (b) polarization curves of Ni_1Co_3–P@CSs $(+)//Ni_1Co_3$–P@CSs $(-)$ and RuO_2/C $(+)//Pt/C$ $(-)$ toward overall water splitting; comparison of cell voltage of Ni_1Co_3–P@CSs $(+)//Ni_1Co_3$–P@CSs $(-)$ with previous reports at J of 50 mA cm^{-2}; (d) time-dependent J curve for $Ni_1Co_3P@CSs$ in a two-electrode configuration at an applied potential of 1.54 V; (e) FE-SEM image of the $Ni_1Co_3P@CSs$ after 38 h stability test; (f) STEM-HAAD of $Ni_1Co_3P@CSs$ coupling with EDS element mapping (Ni, Co, and P) after 40 h stability test.

result is also much better than those of many early reported catalysts (Fig. 7c) [10,60–70]. In addition, the Ni_1Co_3–P@CSs $(+)//Ni_1Co_3$–P@CSs $(-)$ achieves higher current density than RuO_2/C $(+)//Pt/C$ $(-)$ at the surveyed potential of 1.6 V. In this regard, the J value is found to be 56 mA cm^{-2} for Ni_1Co_3–P@CSs $(+)//Ni_1Co_3$–P@CSs $(-)$ while it is only 54 mA cm^{-2} for RuO_2/C $(+)//Pt/C$ $(-)$. Furthermore, the Ni_1Co_3–P@CSs $(+)//Ni_1Co_3$–P@CSs $(-)$ system also displays outstanding durability with a negligible change of current density for 38 h (Fig. 7d), whereas there is a significant change of current density for RuO_2/C $(+)//Pt/C$ $(-)$ after stability testing. This implies the lower stability of RuO_2/C $(+)//Pt/C$ $(-)$ toward water splitting as compared to Ni_1Co_3–P@CSs $(+)//Ni_1Co_3$–P@CSs $(-)$. To further verify the strength of the materials, the phase and morphology of the Ni_1Co_3–P@CSs after stability were investigated by SEM and STEM-HAADF coupling with EDS color mapping. No distinct alteration of macro and micro-characteristics occurs in comparison to the original morphology after working for long time (Fig. 7e). In addition, the phase as well as element dispersion are well maintained with no noticeable changes (Fig. 7f). The result confirms that the Ni_1Co_3–P@CSs $(+)//Ni_1Co_3$–P@CSs $(-)$ can exhibit not only good catalytic activity but also excellent stability for the long-term water splitting process. In another regard, to investigate the effect of pH environment on the catalytic performance of the electrolyzer based on Ni_1Co_3–P@CSs catalyst toward overall water splitting, a 5.3 M KOH electrolyte (30 wt%), which is widely used for commercial water electrolyzer, was applied. Fig. S13a shows that the cell voltage of the electrolyzer is around 1.54 and 1.67 V at 50 and 100 mA cm^{-2}, respectively, significantly better than those of the electrolyzer running in 0.1 M KOH solution (1.54 and 1.8 V at 50 and 100 mA cm^{-2}). However, the electrolyzer running in 5.3 M KOH has lower stability as compared with its operation in 0.1 M KOH (Fig. S13b).

4. Conclusion

A facile strategy was economically developed for the synthesis of an effective catalyst based on bimetallic Ni–Co phosphide nanoneedle

arrays with optimized composition supported on micro-CSs. The Ni_1Co_3–P@CSs catalyst exhibits excellent catalysis toward HER and OER in comparison to its oxide and hydroxide counterparts, as well as Ni–P@CSs, Co–P@CSs, Ni_1Co_2–P@CSs, and Ni_1Co_4–P@CSs in alkaline medium. The HER behavior of the Ni_1Co_3–P@CSs is close to that of Pt/C, but its OER behavior is much better than that of RuO_2/C material. In particular, the practical water splitting application in a two-electrode system shows the superior performance of the Ni_1Co_3–P@CSs $(+)//Ni_1Co_3$–P@CSs $(-)$ compared to RuO_2/C $(+)//Pt/C$ $(-)$ in terms of overpotential, onset overpotential, current density, and durability. The excellent performance of the Ni_1Co_3–P@CSs catalyst may be due to the synergistic effects of Co, Ni, and P, which are uniquely combined to produce exclusive nanoneedle nanoarchitectures vertically growing over the surfaces of CSs. This modulates the electronic structure of the catalyst and enhances the exposed electroactive sites for tuning adsorption energy of the reactants. In addition, the large surface area and good conductivity also provide an important role due to the provision of more channels and shortened partway for fast charge and mass transport. The excellent performance of the Ni_1Co_3–P@CSs suggests it as a potential candidate for practical water splitting application.

Acknowledgements

Appendix A. Supplementary data

Supplementary data associated with this article can be found, in the online version, at https://doi.org/10.1016/j.apcatb.2019.04.017.

References

[1] A. Kudo, Y. Miseki, Heterogeneous photocatalyst materials for water splitting, Chem. Soc. Rev. 38 (2009) 253–278, https://doi.org/10.1039/b800489g.
[2] T. Reier, M. Oezaslan, P. Strasser, Electrocatalytic Oxygen Evolution Reaction

(OER) on Ru, Ir, and Pt catalysts: A comparative study of nanoparticles and bulk materials, ACS Catal. 2 (2012) 1765–1772, https://doi.org/10.1021/cs3003098.

[3] D.T. Tran, T. Kshetri, D.C. Nguyen, J. Gautam, V.H. Hoa, H.T. Le, N.H. Kim, J.H. Lee, Emerging core–shell nanostructured catalysts of transition metal encapsulated by two-dimensional carbon materials for electrochemical applications, Nano Today (2018), https://doi.org/10.1016/j.nantod.2018.08.006.

[4] J. Li, H. Tang, Y. Wang, Z. Huang, J. Zhong, Thermally oxidation synthesis of CuO nanoneedles on Cu foam and its enhanced lithium storage performance, J. Mater. Sci. Mater. Electron. 28 (2017) 2353–2357, https://doi.org/10.1007/s10854-016-5803-8.

[5] E.J. Popczun, C.G. Read, C.W. Roske, N.S. Lewis, R.E. Schaak, Highly active electrocatalysis of the hydrogen evolution reaction by cobalt phosphide nanoparticles, Angew. Chem. Int. Ed. 53 (2014) 5427–5430, https://doi.org/10.1002/anie.402646.

[6] S.T. Oyama, Novel catalysts for advanced hydroprocessing: Transition metal phosphides, J. Catal. 216 (2003) 343–352, https://doi.org/10.1016/S0021-9517(02)00069-6.

[7] J. Tian, Q. Liu, A.M. Asiri, X. Sun, Self-supported nanoporous cobalt phosphide nanowire arrays: An efficient 3D hydrogen-evolving cathode over the wide range of pH 0–14, J. Am. Chem. Soc. 136 (2014) 7587–7590, https://doi.org/10.1021/ja503372r.

[8] C.S. Jung, K. Park, Y. Lee, I.H. Kwak, I.S. Kwon, J. Kim, J. Seo, J.P. Ahn, J. Park, Nickel phosphide polymorphs with an active (0 0 1) surface as excellent catalysts for water splitting, CrystEngComm 21 (2019) 1143–1149, https://doi.org/10.1039/C8CE01884G.

[9] R. Prins, M.E. Bussell, Metal phosphides: Preparation, characterization and catalytic reactivity, Catal Lett. 142 (2012) 1413–1436, https://doi.org/10.1007/s10562-012-0929-7.

[10] H. Liang, A.N. Gandi, D.H. Anjum, X. Wang, U. Schwingenschlögl, H.N. Alshareef, Plasma-assisted synthesis of NiCoP for efficient overall water splitting, Nano Lett. 16 (2016) 7718–7725, https://doi.org/10.1021/acs.nanolett.6b03803.

[11] D.Y. Chung, S.W. Jun, G. Yoon, H. Kim, J.M. Yoo, K.S. Lee, T. Kim, H. Shin, A.K. Sinha, S.G. Kwon, K. Kang, T. Hyeon, Y.E. Sung, Large-scale synthesis of carbon-shell-coated FeP nanoparticles for robust hydrogen evolution reaction electrocatalyst, J. Am. Chem. Soc. 139 (2017) 6669–6674, https://doi.org/10.1021/jacs.7b01530.

[12] Y. Li, H. Zhang, M. Jiang, Y. Kuang, X. Sun, X. Duan, Ternary NiCoP nanosheet arrays: An excellent bifunctional catalyst for alkaline overall water splitting, Nano Res. 9 (2016) 2251–2259, https://doi.org/10.1007/s12274-016-1112-z.

[13] R. Zhang, X. Wang, S. Yu, T. Wen, X. Zhu, F. Yang, X. Sun, X. Wang, W. Hu, Ternary NiCo$_2$P$_x$ nanowires as pH-universal electrocatalysts for highly efficient hydrogen evolution reaction, Adv. Mater. 29 (2017) 1605502, https://doi.org/10.1002/adma.201605502.

[14] J. Li, M. Yan, X. Zhou, Z.Q. Huang, Z. Xia, C.R. Chang, Y. Ma, Y. Qu, Mechanistic insights on ternary Ni$_{2-x}$Co$_x$P for hydrogen evolution and their hybrids with graphene as highly efficient and robust catalysts for overall water splitting, Adv. Funct. Mater. 26 (2016) 6785–6796, https://doi.org/10.1002/adfm.201601420.

[15] J. Li, G. Zheng, One-dimensional earth-abundant nanomaterials for water-splitting electrocatalysts, Adv. Sci. 4 (2017), https://doi.org/10.1002/advs.201600380.

[16] C. Koenigsmann, S.S. Wong, One-dimensional noble metal electrocatalysts: A promising structural paradigm for direct methanol fuel cells, Energy Environ. Sci. 4 (2011) 1161–1176, https://doi.org/10.1039/c0ee00197j.

[17] W. Li, X. Gao, X. Wang, D. Xiong, P.P. Huang, W.G. Song, X. Bao, L. Liu, From water reduction to oxidation: Janus Co–Ni–P nanowires as high-efficiency and ultrastable electrocatalysts for over 3000 h water splitting, J. Power Sources 330 (2016) 156–166, https://doi.org/10.1016/j.jpowsour.2016.08.126.

[18] W. Lu, X. Jiang, L. He, A.M. Asiri, R. Zhang, C. Tang, X. Sun, Fe-doped CoP nanoarray: A monolithic multifunctional catalyst for highly efficient hydrogen generation, Adv. Mater. 29 (2016) 1–6, https://doi.org/10.1002/adma.201602441.

[19] Q. Wang, B. Liu, X. Wang, S. Ran, L. Wang, D. Chen, G. Shen, Morphology evolution of urchin-like NiCo$_2$O$_4$ nanostructures and their applications as psuedocapacitors and photoelectrochemical cells, J. Mater. Chem. 22 (2012) 21647–21653, https://doi.org/10.1039/c2jm34705a.

[20] T.Y. Ma, S. Dai, S.Z. Qiao, Self-supported electrocatalysts for advanced energy conversion processes, Mater. Today 19 (2016) 265–273, https://doi.org/10.1016/j.mattod.2015.10.012.

[21] A. Boudjemaa, A. Rebahi, B. Terfassa, R. Chebout, T. Mokrani, K. Bachari, N.J. Coville, Fe$_2$O$_3$/carbon spheres for efficient photo-catalytic hydrogen production from water and under visible light irradiation, Sol. Energy Mater. Sol. Cells 140 (2015) 405–411, https://doi.org/10.1016/j.solmat.2015.04.036.

[22] C. Huang, T. Ouyang, Y. Zou, N. Li, Z.-Q. Liu, Ultrathin NiCo$_2$P$_x$ nanosheets strongly coupled with CNTs as efficient and robust electrocatalysts for overall water splitting, J. Mater. Chem. A 6 (2018) 7420–7427, https://doi.org/10.1039/C7TA11364A.

[23] C. Galeano, J.C. Meier, M. Soorholtz, H. Bongard, C. Baldizzone, K.J.J. Mayrhofer, F. Schüth, Nitrogen-doped hollow carbon spheres as a support for platinum-based electrocatalysts, ACS Catal. 4 (2014) 3856–3868, https://doi.org/10.1021/cs5003492.

[24] J. Liu, S.Z. Qiao, H. Liu, J. Chen, A. Orpe, D. Zhao, G.Q. Lu, Extension of the stöber method to the preparation of monodisperse resorcinol–formaldehyde resin polymer and carbon spheres, Angew. Chem. Int. Ed. 50 (2011) 5947–5951, https://doi.org/10.1002/anie.201102011.

[25] J. Ryu, Y.W. Suh, D.J. Suh, D.J. Ahn, Hydrothermal preparation of carbon microspheres from mono-saccharides and phenolic compounds, Carbon 48 (2010) 1990–1998, https://doi.org/10.1016/j.carbon.2010.02.006.

[26] M. Li, W. Li, S. Liu, Hydrothermal synthesis, characterization, and KOH activation of carbon spheres from glucose, Carbohydr. Res. 346 (2011) 999–1004, https://doi.org/10.1016/j.carres.2011.03.020.

[27] A.H. Lu, W.C. Li, G.P. Hao, B. Spliethoff, H.J. Bongard, B.B. Schaack, F. Schüth, Easy synthesis of hollow polymer, carbon, and graphitized microspheres, Angew. Chem. Int. Ed. 49 (2010) 1615–1618, https://doi.org/10.1002/anie.200906445.

[28] T. Yang, J. Liu, R. Zhou, Z. Chen, H. Xu, S.Z. Qiao, M.J. Monteiro, N-doped mesoporous carbon spheres as the oxygen reduction reaction catalysts, J. Mater. Chem. A 2 (2014) 18139–18146, https://doi.org/10.1039/c4ta04301d.

[29] H. Mao, X. Chen, R. Huang, M. Chen, R. Yang, P. Lan, M. Zhou, F. Zhang, Y. Yang, X. Zhou, Fast preparation of carbon spheres from enzymatic hydrolysis lignin: Effects of hydrothermal carbonization conditions, Sci. Rep. 8 (2018) 2–11, https://doi.org/10.1038/s41598-018-27777-4.

[30] X. Xia, Y. Wang, D. Wang, Y. Zhang, Z. Fan, J. Tu, H. Zhang, H.J. Fan, Atomic-layer-deposited iron oxide on arrays of metal/carbon spheres and their application for electrocatalysis, Nano Energy 20 (2016) 244–253, https://doi.org/10.1016/j.nanoen.2015.12.015.

[31] J. Cheng, Y. Wang, C. Teng, Y. Shang, L. Ren, B. Jiang, Preparation and characterization of monodisperse, micrometer-sized, hierarchically porous carbon spheres as catalyst support, Chem. Eng. J. 242 (2013) 285–293, https://doi.org/10.1016/j.cej.2013.12.089.

[32] S. Dutta, A. Indra, Y. Feng, T. Song, U. Paik, Self-supported nickel iron layered double hydroxide-nickel selenide electrocatalyst for superior water splitting activity, ACS Appl. Mater. Interf. 9 (2017) 33766–33774, https://doi.org/10.1021/acsami.7b07984.

[33] L. Ai, Z. Niu, J. Jiang, Mechanistic insight into oxygen evolution electrocatalysis of surface phosphate modified cobalt phosphide nanorod bundles and their superior performance for overall water splitting, Electrochim. Acta 242 (2017) 355–363, https://doi.org/10.1016/j.electacta.2017.05.032.

[34] Y. Pan, W. Hu, D. Liu, Y. Liu, C. Liu, Carbon nanotubes decorated with nickel phosphide nanoparticles as efficient nanohybrid electrocatalysts for the hydrogen evolution reaction, J. Mater. Chem. A 3 (2015) 13087–13094, https://doi.org/10.1039/c5ta02128f.

[35] X. Xiao, L. Tao, M. Li, X. Lv, D. Huang, X. Jiang, H. Pan, M. Wang, Y. Shen, Electronic modulation of transition metal phosphide: Via doping as efficient and pH-universal electrocatalysts for hydrogen evolution reaction, Chem. Sci. 9 (2018) 1970–1975, https://doi.org/10.1039/c7sc04849a.

[36] D. Lee, Q.X. Xia, J.M. Yun, K.H. Kim, High-performance cobalt carbonate hydroxide nano-dot/NiCo(CO$_3$)(OH)$_2$ electrode for asymmetric supercapacitors, Appl. Surf. Sci. 433 (2018) 16–26, https://doi.org/10.1016/j.apsusc.2017.10.066.

[37] Q. Cheng, S. Xu, X. Wang, C. Guo, Ionic liquid-coated nickel phosphide catalysts for selective hydrodesul-furization, Chem. Eng. Technol. 36 (2013) 228–232, https://doi.org/10.1002/ceat.201200423.

[38] Y. Pan, Y. Liu, J. Zhao, K. Yang, J. Liang, D. Liu, W. Hu, D. Liu, Y. Liu, C. Liu, Monodispersed nickel phosphide nanocrystals with different phases: Synthesis, characterization and electrocatalytic properties for hydrogen evolution, J. Mater. Chem. A 3 (2015) 1656–1665, https://doi.org/10.1039/c4ta04867a.

[39] Y. Pan, Y. Lin, Y. Chen, Y. Liu, C. Liu, Cobalt phosphide-based electrocatalysts: synthesis and phase catalytic activity comparison for hydrogen evolution, J. Mater. Chem. A 4 (2016) 4745–4754, https://doi.org/10.1039/c6ta00575f.

[40] Y. Zheng, C. Gao, W. Kuang, Y. Zhu, A. Huczko, M. Bystrzejewski, M. Roe, C. Young, S. Acquah, H. Kroto, D.R.M. Walton, Large-scale synthesis and characterization of carbon spheres prepared by direct pyrolysis of hydrocarbons, Carbon 43 (2005) 1944–1953, https://doi.org/10.1016/j.carbon.2005.03.002.

[41] B. Zhang, Y. Hui, H. Ni, S. Hu, Bimetallic (Fe$_x$Ni$_{1-x}$)$_2$P nanoarrays as exceptionally efficient electrocatalysts for oxygen evolution in alkaline and neutral media, Nano Energy 38 (2017) 553–560, https://doi.org/10.1016/j.nanoen.2017.06.032.

[42] A.A. Mirghni, M.J. Madito, K.O. Oyedotun, T.M. Masikhwa, N.M. Ndiaye, A high energy density asymmetric supercapacitor utilizing a nickel phosphate/graphene foam composite as the cathode and carbonized iron, RSC Adv. 8 (2018) 11608–11621, https://doi.org/10.1039/c7ra12028.

[43] P.F. Liu, X. Li, S. Yang, M.Y. Zu, P. Liu, B. Zhang, L.R. Zheng, H. Zhao, H.G. Yang, Ni$_2$P(O)/Fe$_2$P(O) interface can boost oxygen evolution electrocatalysis, ACS Energy Lett. 2 (2017) 2257–2263, https://doi.org/10.1021/acsenergylett.7b00638.

[44] A.W. Burns, K.A. Layman, D.H. Bale, M.E. Bussell, Understanding the relationship between composition and hydrodesulfurization properties for cobalt phosphide catalysts, Appl. Catal. A: Gen. 343 (2008) 68–76, https://doi.org/10.1016/j.apcata.2008.03.022.

[45] Z. Huang, Z. Chen, Z. Chen, C. Lv, M.G. Humphrey, C. Zhang, Cobalt phosphide nanorods as an efficient electrocatalyst for the hydrogen evolution reaction, Nano Energy 9 (2014) 373–382, https://doi.org/10.1016/j.nanoen.2014.08.013.

[46] W. Li, Q. Yang, S. Chou, J. Wang, H. Liu, Cobalt phosphide as a new anode material for sodium storage, J. Power Sources 294 (2015) 627–632, https://doi.org/10.1016/j.jpowsour.2015.06.097.

[47] X. Wang, W. Li, D. Xiong, D.Y. Petrovykh, L. Liu, Bifunctional nickel phosphide nanocatalysts supported on carbon fiber paper for highly efficient and stable overall water splitting, Adv. Funct. Mater. 26 (2016) 4067–4077, https://doi.org/10.1002/adfm.201505509.

[48] C.-Z. Yuan, Y.-F. Jiang, Z. Wang, X. Xie, Z.-K. Yang, A. Bin Yousaf, A.-W. Xu, Cobalt phosphate nanoparticles decorated with nitrogen-doped carbon layers as highly active and stable electrocatalysts for the oxygen evolution reaction, J. Mater. Chem. A. 4 (2016) 8155–8160, https://doi.org/10.1039/C6TA01929C.

[49] X. Fan, C. Yu, Z. Ling, J. Yang, J. Qiu, Hydrothermal synthesis of phosphate-functionalized carbon nanotube-containing carbon composites for supercapacitors with highly stable performance, ACS Appl. Mater. Interf. 5 (2013) 2104–2110, https://doi.org/10.1021/am303052n.

[50] A. Walcarius, Mesoporous materials and electrochemistry, Chem. Soc. Rev. 42 (2013) 4098–4140, https://doi.org/10.1039/c2cs35322a.

[51] J. Liang, Y. Jiao, M. Jaroniec, S.Z. Qiao, Sulfur and nitrogen dual-doped mesoporous graphene electrocatalyst for oxygen reduction with synergistically enhanced performance, Angew. Chem. 124 (2012) 11664–11668, https://doi.org/10.1002/ange.201206720.

[52] G.J. Kubas, Fundamentals of H_2 binding and reactivity on transition metals underlying hydrogenase function and H_2 production and storage, Chem. Rev. 107 (2007) 4152–4205, https://doi.org/10.1021/cr050197j.

[53] Y. Zhang, Q. Shao, S. Long, X. Huang, Cobalt-molybdenum nanosheet arrays as highly efficient and stable earth-abundant electrocatalysts for overall water splitting, Nano Energy 45 (2018) 448–455, https://doi.org/10.1016/j.nanoen.2018.01.022.

[54] N. Mahmood, Y. Yao, J.W. Zhang, L. Pan, X. Zhang, J.J. Zou, Electrocatalysts for hydrogen evolution in alkaline electrolytes: mechanisms, challenges, and prospective solutions, Adv. Sci. 5 (2018) 1700464, https://doi.org/10.1002/advs.201700464.

[55] C. Dong, X. Yuan, X. Wang, X. Liu, W. Dong, R. Wang, Rational design of cobalt–chromium layered double hydroxide as a highly efficient electrocatalyst for water oxidation, J. Mater. Chem. A 4 (2016) 11292–11298, https://doi.org/10.1039/c6ta04052g.

[56] Y. Liu, A.Z. Fire, S. Boyd, R.A. Olshen, Mechanistic studies of the oxygen evolution reaction by a cobalt-phosphate catalyst at neutral pH, J. Am. Chem. Soc. 132 (2010) 16501–16509, https://doi.org/10.1021/ja908730h.(45).

[57] L.A. Stern, L. Feng, F. Song, X. Hu, Ni_2P as a Janus catalyst for water splitting: The oxygen evolution activity of Ni_2P nanoparticles, Energy Environ. Sci. 8 (2015) 2347–2351, https://doi.org/10.1039/c5ee01155h.

[58] J. Ryu, N. Jung, J.H. Jang, H.J. Kim, S.J. Yoo, In situ transformation of hydrogen-evolving CoP nanoparticles: Toward efficient oxygen evolution catalysts bearing dispersed morphologies with Co-oxo/hydroxo molecular units, ACS Catal. 5 (2015) 4066–4074, https://doi.org/10.1021/acscatal.5b00349.

[59] A. Dutta, N. Pradhan, Developments of metal phosphides as efficient OER precatalysts, J. Phys. Chem. Lett. 8 (2017) 144–152, https://doi.org/10.1021/acs.jpclett.6b02249.

[60] Y. Jia, L. Zhang, G. Gao, H. Chen, B. Wang, J. Zhou, M.T. Soo, A heterostructure coupling of exfoliated Ni–Fe hydroxide nanosheet and defective graphene as a bifunctional electrocatalyst for overall water splitting, Adv. Mater. 29 (2017) 1–8, https://doi.org/10.1002/adma.201700017.

[61] M. Gong, W. Zhou, M. Tsai, J. Zhou, M. Guan, M. Lin, B. Zhang, Y. Hu, D. Wang, J. Yang, S.J. Pennycook, B. Hwang, H. Dai, Nanoscale nickel oxide/nickel heterostructures for active hydrogen evolution electrocatalysis, Nat. Commun. 5 (2014) 1–6 doi:10.1038/ncomms5695.

[62] Y. Tan, H. Wang, P. Liu, Y. Shen, C. Cheng, Versatile nanoporous bimetallic phosphides towards electrochemical water splitting, Energy Environ. Sci. 9 (2016) 2257–2261, https://doi.org/10.1039/c6ee01109h.

[63] H. Wang, H. Lee, Y. Deng, Z. Lu, P. Hsu, Y. Liu, D. Lin, Y. Cui, Bifunctional non-noble metal oxide nanoparticle electrocatalysts through lithium-induced conversion for overall water splitting, Nat. Commun. 6 (2015) 1–8, https://doi.org/10.1038/ncomms8261.

[64] N. Jiang, B. You, M. Sheng, Y. Sun, Electrodeposited cobalt-phosphorous-derived films as competent bifunctional catalysts for overall water splitting, Chem. Int. Ed. 54 (2015) 6251–6254, https://doi.org/10.1002/anie.201501616.

[65] X. Gao, H. Zhang, Q. Li, X. Yu, Z. Hong, X. Zhang, C. Liang, Z. Lin, Water splitting hot paper hierarchical $NiCo_2O_4$ hollow microcuboids as bifunctional electrocatalysts for overall water-splitting, Angew. Chem. Int. Ed. 55 (2016) 6290–6294, https://doi.org/10.1002/anie.201600525.

[66] L. Feng, G. Yu, Y. Wu, G. Li, H. Li, Y. Sun, T. Asefa, W. Chen, X. Zou, High-index faceted Ni_3S_2 nanosheet arrays as highly active and ultrastable electrocatalysts for water splitting, J. Am. Chem. Soc. 137 (2015) 3–6, https://doi.org/10.1021/jacs.5b08186.

[67] L. Yu, H. Zhou, J. Sun, F. Qin, F. Yu, J. Bao, Cu nanowires shelled with NiFe layered double hydroxide nanosheets as bifunctional electrocatalysts for overall water splitting, Energy Environ. Sci. 10 (2017) 1820–1827, https://doi.org/10.1039/c7ee01571b.

[68] B. You, Y. Sun, Hierarchically porous nickel sulfi de multifunctional superstructures, Adv. Energy Mater. 6 (2016) 1–7, https://doi.org/10.1002/aenm.201502333.

[69] J. Yu, Q. Li, Y. Li, C. Xu, L. Zhen, V.P. Dravid, Ternary metal phosphide with triple-layered structure as a low-cost and effi cient electrocatalyst for bifunctional water splitting, Adv. Funct. Mater. 26 (2016) 7644–7651, https://doi.org/10.1002/adfm.201603727.

[70] Y. Zhu, Y. Liu, T. Ren, Z. Yuan, Self-supported cobalt phosphide mesoporous nanorod arrays: a flexible and bifunctional electrode for highly active electrocatalytic water reduction and oxidation, Adv. Funct. Mater. 25 (2015) 7337–7347, https://doi.org/10.1002/adfm.201503666.